

# Two-Dimensional Crystallization of Hexagonal Bilayer with Moiré Patterns

Z. G. Chen,<sup>†,#</sup> Z. P. Xu,<sup>†,#</sup> M. Zhang,<sup>‡</sup> Y. Zhou,<sup>§</sup> M. Liu,<sup>||</sup> T. Patten,<sup>‡</sup> G.-Y. Liu,<sup>‡</sup> H. Li,<sup>⊥</sup> X. C. Zeng,<sup>\*,⊥</sup> and L. Tan<sup>\*,†,⊥</sup>

<sup>†</sup>Department of Mechanical and Materials Engineering and Nebraska Center for Materials and Nanoscience, University of Nebraska, Lincoln, Nebraska 68588, United States

<sup>‡</sup>Department of Chemistry, University of California, Davis, California 95616, United States

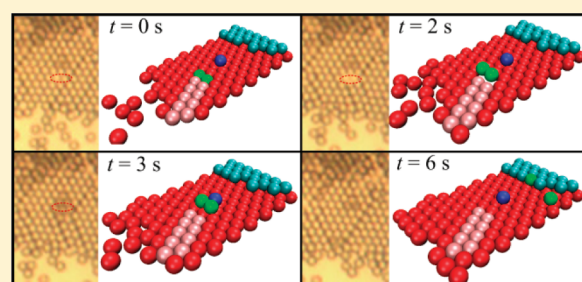
<sup>§</sup>Center for Biotechnology, University of Nebraska, Lincoln, Nebraska 68588, United States

<sup>||</sup>Agilent Technologies Inc., 5301 Stevens Creek Boulevard, Santa Clara, California 95051, United States

<sup>⊥</sup>Department of Chemistry, University of Nebraska, Lincoln, Nebraska 68588, United States

## Supporting Information

**ABSTRACT:** Direct observation of crystallization dynamics in real space is of special interest to scientists in various disciplines. Although direct observation of transient structural transformation in a nanocrystalline system has been recently achieved using the state-of-the-art aberration-corrected transmission electron microscopy (AC-TEM), the small length scales of individual species in molecular systems still preclude routine observation of crystallization dynamics. Unidirectional packing of microbeads can serve as an experimental model system, as their dynamics can be observed and recorded readily in the laboratory due to their larger size and slower time scale. Herein, we present direct observation of a two-dimensional (2D) crystallization enabled by such a packing process. The direct imaging approach not only allows observation of the dynamics in a bead-by-bead fashion but also reveals intriguing phenomena, such as the formation of grain boundaries, disorder–order transitions, and the Moiré patterns which arise when two periodic monolayers are overlaid at certain angles. In addition, the imaging afforded by confocal microscopy facilitates a structural analysis of height-dependent polygonal tiling of the top monolayer, which has implication to the formation of 2D quasicrystals.



## 1. INTRODUCTION

Crystallization is a classical example of the first-order phase transition<sup>1–3</sup> and is ubiquitous in nature. An understanding of microscopic processes in crystallization is of both fundamental and practical importance for controlling the ordering and growth of crystals. Direct observation of real-space crystallization in real time offers a powerful way to gain deeper insights into the crystallization kinetics as well as into other rarely observed phenomena, such as dislocation motion and grain-boundary formations. Recently, an *in situ* observation of trajectories of structural transformations in a single nanorod with atomic resolution has been achieved by Zheng et al. using AC-TEM.<sup>4</sup> However, the small length scales of individual species in these nanocrystalline systems still preclude routine observation of crystallization dynamics. On the other hand, micrometer-sized colloids or beads can function as scale-up model systems for the study and direct observation of dynamics of crystal nucleation and growth.<sup>5–13</sup>

In this study, we focus on 2D crystallization of a hexagonal bilayer using micrometer spheres (dubbed microbeads) as the model system. To this end, we have designed a new instrument (see Supporting Information Figure S1) based on the

controlled-drying technique previously developed for 2D colloidal crystallization.<sup>10,13</sup> In this technique, crystal formation is driven by a unidirectional fluid flow which is induced by liquid evaporation. Two unique features in our newly designed instrument are as follows: (1) A slit micropore is used to confine and control the fluid flow into a capillary flow, rather than using an open-ended substrate for drying<sup>13</sup> so that the thickness of the 2D crystal can be controlled accordingly. (2) The 2D crystal grows inside the fluid, in the direction opposite to the capillary flow rather than at the drying front of an evaporation.<sup>11,13</sup> Owing to the micrometer length scale of the microbeads, and the time scale of crystallization in seconds, direct observation of the crystal growth in real time is feasible through conventional microscopy. Herein, for the first time, coexistence of various Moiré patterns within the same bilayer crystal is observed. Such patterns have recently received a resurgence of interest in materials science due to the observation of Moiré-pattern-dependent electronic properties

Received: November 25, 2011

Revised: February 7, 2012

Published: February 22, 2012

in stacked graphene sheets at different angles,<sup>14,15</sup> and the scanning tunneling microscopy (STM) imaging of Moiré patterns produced by a graphene sheet on hexagonal boron nitride.<sup>16</sup> Moiré patterns have also been directly observed in polystyrene latex bilayers by optical microscopy.<sup>17</sup>

In addition to the crystalline morphologies and Moiré patterns, 2D tiling of the particles at different slicing planes can be further investigated by laser confocal microscopy. Here, we also present such a tiling of the microbeads at different heights, particularly for the Moiré pattern at  $\sim 30^\circ$  rotational angle. Interestingly, we find that, within a certain range of heights, the tiling of the beads exhibits disordered equilateral triangles and rectangles surrounded by those triangle tiles, including fragments of 3<sup>2</sup>.4.3.4 Archimedean tiling.<sup>18–21</sup> The simulated diffraction patterns suggest that the tiling exhibits 12-fold (dodecagonal) symmetry. Note that a variety of quasi-periodic tiling patterns with high symmetry have been observed in a metal alloy,<sup>18</sup> 2D Lennard-Jones model particles,<sup>20</sup> a supramolecular micellar phase,<sup>22</sup> star polymers,<sup>23</sup> a colloid monolayer,<sup>24</sup> binary nanoparticle superlattices,<sup>25</sup> a densely packed tetrahedral,<sup>26</sup> and stacked hexagonal layers of micelles.<sup>27</sup> Hence, this latter study on the height-dependent tiling of the particles, on the basis of the stacked hexagonal model system, may provide a better understanding of 2D quasi-periodicity with a 12-fold diffraction symmetry. Since our reported features here are constructed with uniform building blocks, this study may have implications for the design of functional materials and devices,<sup>28–33</sup> such as nanostructures for catalysis and electronics, subwavelength structures for photonics, and metamaterials.

## 2. MATERIALS AND METHODS

**Bilayer Crystal Growth.** The crystal growth is initiated by a unidirectional drying of an aqueous suspension of silica microbeads through a slit pore. The suspension is prepared by adding beads into distilled water at a concentration of 2.0 wt %, followed by sonicating the solution for 10 min. The resulting solution is then dropped over a clean glass substrate, with another glass slide capping the droplet and spacers to control the gap between the two solid surfaces (see Figure S1, Supporting Information).

**Characterization.** The optical microscope used for imaging is ML8000 Meiji equipped with a digital camera (Moticam 2000). Laser confocal images are taken using an inverted (Olympus IX 81) confocal microscope. The Moticam 2000 has image-analysis software, which provides domain size information on captured Moiré features.

## 3. RESULTS AND DISCUSSION

A schematic illustration of our experimental concept and setup is shown in Figure 1A and Figure S1 (Supporting Information), respectively. In this controlled-drying device, nearly uniform microbeads with a diameter of  $2.6\ \mu\text{m}$  are initially suspended in a confined aqueous environment between two glass surfaces. As shown in Figure 1A, the row-by-row stacking of the microbeads occurs only on the right side of the setup once water starts evaporation. As such, the microbeads, moving from the left side toward the drying front, form a hexagonal monolayer in the early stage of the evaporation. Once the hexagonal monolayer reaches a critical width, the capillary flow then leads to stacking and forming of a bilayer structure, where microbeads of the top layer are found not necessarily located within the hollow sites

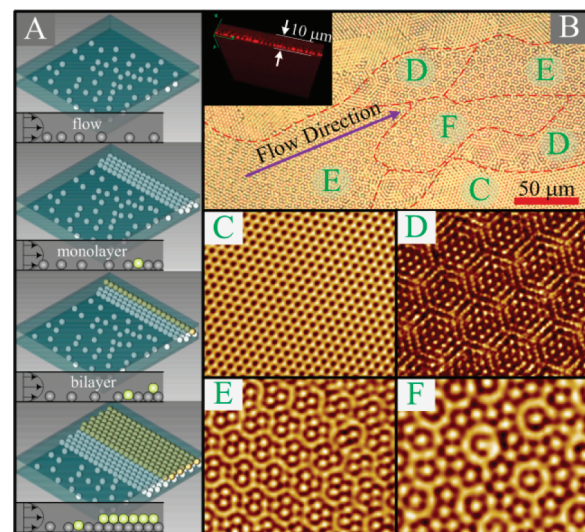


**Figure 1.** (A) Schematic plots of sequenced growth of a hexagonal bilayer crystal via a unidirectional capillary flow. A droplet of solvated micrometer-scale beads (2 wt % in water) is first placed between two glass plates and confined by additional solid spacers in the horizontal plane. The row-by-row stacking for the dispersed microbeads proceeds by letting water evaporate from the slit pore only. (B) Optical microscopy image of the formed bilayer crystal, where grain or domain boundaries are highlighted with dashed lines in red. The longitudinal direction of the polymorph is along the capillary flow direction. The laser confocal microscopy image in the inset shows a thickness of  $10\ \mu\text{m}$  between the two glass plates, as well as a side view of tightly packed beads. (C–F) Zoom-in features of different domains inside the bilayer crystal.

of the bottom layer. Figure 1B shows optical images of multiple bilayer structures or bilayer polymorphs. These bilayer polymorphs differ by the rotation angle between the top and bottom layers. It also appears that these bilayer polymorphs are more or less equally stable and thus can coexist together. Analogous to the Moiré phenomena,<sup>17,34–36</sup> these observed patterns can be regarded as overlaying two close-packed but optically translucent monolayers (see Figure S2, Supporting Information). If the rotation angle varies from  $10$  to  $30^\circ$ , not only has it shown a continuously changing symmetry in the bilayer packing, but also the periodicity reduces as the increase of the rotation angle. Specifically, when the top layer sits exactly in the triple hollow sites of the bottom monolayer, a perfectly closed-packed bilayer phase is formed, as shown in Figure 1C, where the rotation angle is  $0^\circ$ . In contrast, when the rotation angle is nonzero, bilayer phases with different superfine structures can be observed, where three selected regions are shown in Figure 1D–F. In Figure 1D and E, the rotation angles are about  $10$  and  $20^\circ$ , where periodic features with superfine structures are clearly visible. The corresponding fast Fourier transform (FFT) patterns of Figure 1D and E are shown in Figure S2 (Supporting Information). More interestingly, when the rotation angle is about  $30^\circ$  (Figure 1F), aperiodic stacking with a dodecagonal symmetry is observed. Overall, different Moiré domains coexist in the single bilayer, which accumulate in a longitudinal stripe whose long dimension is in the direction of drying or capillary flow (see Figure 1B).

To gain more quantitative insights into the observed Moiré patterns, we have performed downhill Monte Carlo simulations of hard-sphere bilayers for which all hard spheres have the same diameter as microbeads. The lateral dimension of the bilayer is

chosen to be  $160 \times 160 \mu\text{m}^2$ , close to a typical Moiré domain observed in our experiment. Details of the simulation system are presented in Figure S3 (Supporting Information). We have performed the simulation of bilayer relaxation at various rotation angles. By comparing Moiré patterns from simulations with the experimental ones, we find that the modeled features at rotation angles of 11, 22, and  $30^\circ$  (see Figure 2A–C) match

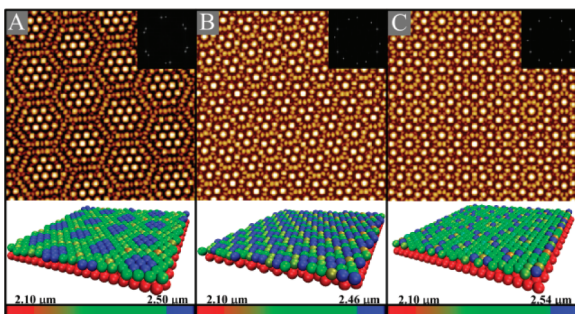


**Figure 2.** (top panel) Simulated optical microscopy images (thickness contrast of microbeads) for three Moiré patterns shown in Figure 1D–F, where the top layer is manually rotated at an angle of (A)  $11^\circ$ , (B)  $22^\circ$ , and (C)  $30^\circ$  with respect to the bottom layer. (bottom panel) 3D illustration of the bilayer crystal, where the beads in the top layer are colored based upon their heights measured from the mass center of the bottom layer (heights are shown in the color bar). Insets: fast Fourier transform (FFT) patterns of the simulated optical images, where bright spots indicate the ordering of the Moiré feature and the angular spacing for rotation angles between neighboring layers. Experimental FFTs are included in Figure S2 of the Supporting Information to show agreement.

those imaged by optical microscopy the best (Figure 1D–F). The agreement is further supported by the consistent FFT patterns of simulation (insets in Figure 2) and experiment (Figure S2, Supporting Information). With the rotation angle being determined, the 3D configurations of realistic microbeads at the corresponding rotation angle can be approximately modeled through the simulation (see the lower panel of Figure 2), where the landscape (or height variation) of the bilayer microbeads is described *via* a color spectrum (red refers to the lowest height, while blue refers to the highest height).

The time-dependent crystal growth process and Moiré patterns can be further investigated through laser confocal microscopy, as shown in Figure 3A. Three snapshots with a time interval of 5 s highlight the growth process, where the top portion of the confocal micrograph denotes a bilayer structure with many microbeads organized in a dodecagonal fashion. At the very bottom rim of the stacks, incoming microbeads form a narrow monolayer, a reflection of sequential growth mode. Meanwhile, there are isolated microbeads moving upward, and in the confocal images, they exhibit elliptical shapes due to the fast motion of the flow. The height variation in the top layer is also made evident by slicing the bilayer at different heights and plotting the image in the transmitted light mode (Figure 3B–E). For instance, when slicing the plane through the mass center of the bottom layer (referred to as  $h = 0 \mu\text{m}$  in Figure 3B), only the bottom layer is scanned to show a uniform size of microbeads and the close-packed hexagonal organization. When the slicing plane is elevated to  $h = 1.2 \mu\text{m}$  (Figure 3C), the confocal micrograph shows that a partial layer from the top is overlaid atop the bottom layer and delivers an optically quasi-periodic pattern with a dodecagonal symmetry. FFT of the as-

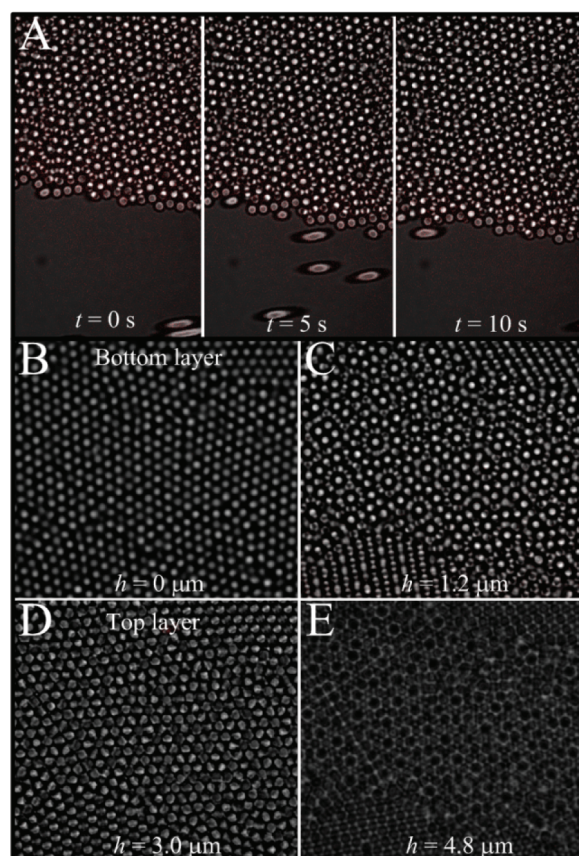


**Figure 3.** (A) Dynamic growth of the bilayer crystal imaged by laser confocal microscopy at different times. A liquid flow in the upward direction pushes the microbeads toward the rim of a monolayer. Both the monolayer and bilayer rims grow in the downward direction. (B–E) Transmitted laser light confocal microscopy images of the bilayer crystal at different slicing planes, where the height ( $h$ ) is calculated as the distance from the mass center of the bottom layer: (B)  $h = 0 \mu\text{m}$ , showing a close-packed hexagonal monolayer (bottom layer); (C)  $h = 1.2 \mu\text{m}$ , showing a cross section of the top layer mixed with the bottom one, giving rise to an apparent dodecagonal symmetry. As the slicing plane is elevated to  $3.0 \mu\text{m}$  (D), or  $4.8 \mu\text{m}$  (E), the top layer catches most of the focus, with a fading contrast for the bottom layer. The diameter of the microbeads is  $2.6 \mu\text{m}$ .

imaged pattern is displayed in Figure S4A (Supporting Information), which confirms the apparent dodecagonal symmetry. However, at the bottom of Figure 3C, there are microbeads grouped together in a parallel fashion (showing striped necklace-like features), suggesting a small translation between both layers in stacking; i.e., some microbeads are located exactly between vacancies of two bottom ones. When the slicing plane is further elevated to  $h = 3.0 \mu\text{m}$  (Figure 3D) and  $4.8 \mu\text{m}$  (Figure 3E), the top layer catches most of the focus, with a fading contrast for the bottom layer. Sizes of the circles shown in Figure 3E vary from location to location, indicating that the microbeads in the top layer are not located in the same plane; namely, those with higher heights exhibit smaller circles and those with lower heights exhibit larger circles. Moreover, by comparing Figure 3B and D, a relative rotation between the top and bottom layers is clearly visible. A simulated laser confocal image of the bilayer at  $h = 1.2 \mu\text{m}$  is shown in Figure S4B (Supporting Information), which supports the experimental observation. The corresponding FFT depicts a 12-fold symmetry as well. If we remove the microbeads underneath

the slicing plane of 2.54 or 2.52  $\mu\text{m}$  (based on the lower panel of Figure 2C), we attain the polygonal tiling, as shown in Figure 4A and B, respectively. Tiles in Figure 4B mainly consist of

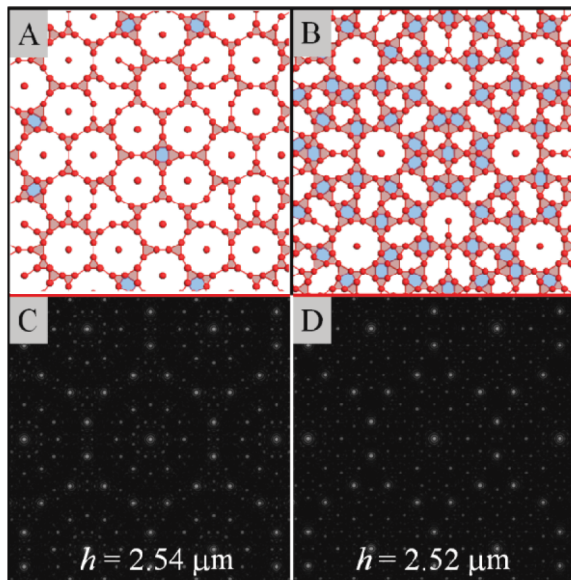


**Figure 4.** When microbeads below the height of (A) 2.54 and (B) 2.52  $\mu\text{m}$  are removed, features with disordered equilateral triangles and rectangles show up, resembling fragments of 3<sup>2</sup>.4.3.4 Archimedean tiling. The height is measured from the mass center of the bottom monolayer. Parts C and D are simulated diffraction patterns of parts A and B, respectively, which show 12-fold symmetry.

equilateral triangles (with different sizes) and rectangles surrounded by four of those triangles, which exhibit no long-range translational ordering.<sup>21,22</sup> The corresponding FFT depicts a 12-fold symmetry, akin to previously discovered 2D quasicrystals with the same symmetry.<sup>37</sup>

The important role of the capillary flow along the liquid–microbeads interface is illustrated in Figure 5A. First and foremost, a capillary flow will generate a 2-D horizontal velocity field between two glass surfaces, as shown in Figure 5A.<sup>38,39</sup> This velocity field,  $u(y) = u_{\max}[1 - (y/H)^2]$ , has a maximum velocity ( $u_{\max}$ ) in the central plane of the slit pore ( $y = 0$ ) but remains stationary next to the two solid surfaces ( $y = \pm H$ ). We can estimate the liquid flow velocity atop one single particle at  $y = D/2 - H$  ( $D$  is the microbead diameter), as well as the flow velocities within the entire capillary gap, by recording the velocity of those mobile microbeads ( $u_r$ ). After the bottom monolayer forms ( $y = -H_1 = D/2 - H$ ), the capillary flow will generate a shear stress,  $\tau \propto (du_1(y)/dy)|_{y=-H_1}$ , or a viscous force,  $f_v = (\pi D^2/4)\tau$ , to each stationary microbead inside the monolayer. We have verified the presence of such a fluid flow above the monolayer by adding an oil droplet into the suspension (see jp211369r\_si\_001.mpg, Supporting Information). Since the oil has a lower density than the water and microbeads, it floats over the packed monolayer and moves toward the drying front. When the liquid dries very slowly or this capillary flow is trivial, the net gravity force (difference between the weight and buoyancy) will be dominant; the microbeads will only be stacked into a close-packed monolayer until the depletion of all the mobile ones. However, in our setup, dispersed microbeads all moved at a velocity of  $\sim 10 \mu\text{m}/\text{s}$ , which roughly produces a viscous force  $f_v \sim 0.09 \text{ pN}$ ,

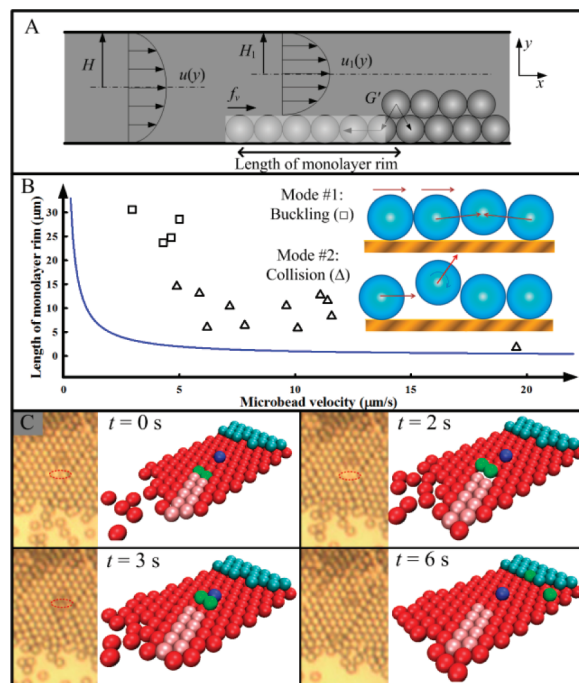


**Figure 5.** (A) Side view illustration of the role of capillary flow to the crystallization of the hexagonal bilayer. A mechanics model of the fluid can be built to calculate the shear stress from capillary flow, and a statics model (see the Supporting Information) for the packed monolayer is built to estimate the length of the monolayer rim. (B) The estimated length of the monolayer rim (blue curve) decreases rapidly with increasing flow velocity. Experimental data largely support this estimation, where moving beads can be divided into two groups in the growth of the crystal. When the capillary flow is slow (low microbead velocity), the bilayer has a very long monolayer rim. Resulting buckling or structural instability inside this monolayer then contributed to the bilayer growth (mode #1). In contrast, when the capillary flow is fast (high microbead velocity), accelerated beads directly jump over the packed monolayer to form the top layer, accompanied with a possible internal rotation for the bead (mode #2) and a rather short monolayer rim. (C) Optical microscopy images (yellow-brown color) captured details of mode #1, where two beads (highlighted by a red circle in the OM image; also denoted by green balls in 3D schematic illustrations) popped up at  $t = 2 \text{ s}$  (lighter color in red circle). At  $t = 3 \text{ s}$ , leftover patches (pink balls) quickly filled the vacancy due to the relocation of the two beads next to the landmark (blue ball). At  $t = 6 \text{ s}$ , the dark spots next to the landmark disappeared, indicating regrouping of the two beads into the top monolayer. Note that a triangular shaped dark spot is positioned above the red circle. This landmark (denoted by blue ball) is located inside a triple hollow site of the bottom monolayer. Other snapshots are available for additional viewing in jp211369r\_si\_001.mpg in the Supporting Information.

comparable to the net gravity force (0.15 pN). Hence, the formation of bilayer crystal is made evident whenever the length of the bottom monolayer rim (Figure 5A) exceeds a critical value, which ranged from one bead in length ( $D$  or 2.6  $\mu\text{m}$ ) for a fast capillary flow (jp211369r\_si\_002.mpg, Supporting Information) or ten beads in length ( $10D$  or 26  $\mu\text{m}$ ) for a relatively slow flow (jp211369r\_si\_003.mpg, Supporting Information). As a consequence, two different mechanisms for the growth of bilayer crystal are identified. When the liquid flows slowly, the crystal growth is attributed to a monolayer buckling mechanism (mode #1, Figure 5B). In this case, because the monolayer rim is fairly wide, microbeads

within the monolayer can be squeezed upward to join the top layer. On the other hand, when the liquid flows relatively fast, incoming microbeads can jump directly over the bottom layer after a collision, accompanied with possible internal rotations (mode #2, Figure 5B). Interestingly, we find that neither of these two modes can trigger the formation of a third layer. It is possible that, when the capillary flow is slow, the bilayer structure itself is already highly intact with exceptional stability due to the interlocking of microbeads. As a result, the buckling mode is ineffective for the bilayer structure, thereby prohibiting the growth of a third layer. When the capillary flow is fast, however, a large number of beads are used in the process of forming the bottom monolayer, with a rather low probability for them colliding with other microbeads from the top layer. We expect that when the flow speed is very high, the third layer will arise. However, in our setup, the flow speed is limited within a small range (Figure 5B) because the evaporation rate is relatively slow at room temperature.

We have also estimated the length of the monolayer rim using a simple statics model (see the Supporting Information and Figure S5). The estimation is largely in good agreement with the observed length reduction as the velocity increases (see the blue curve in Figure 5B). Since the crystal growth mechanism is dependent on the flow velocity, the data points are well separated into two groups, with longer rims for the buckling mode and shorter rims for the collision mode. Furthermore, to have a clearer insight into the role of the buckling-based growth mode, we depict schematic 3D models next to the experimental images in Figure 5C. Specifically, two beads have been found popping up in the middle of a monolayer at  $t = 2$  s, then the capillary flow pushed the neighboring patches (highlighted by pink,  $t = 3$  s) to fill the vacancy, followed by the two extra beads joining in the top layer ( $t = 6$  s).

While the growth of the bilayer crystal has largely been attributed to the capillary flow, it is yet unclear how multiple Moiré features are packed side by side in the same crystal. To elucidate this, we manually extracted the coordinates of packed beads from Figure 3B and D and replotted them in Figure 6A as two neighboring layers of perfect spheres. Mainly, the top spheres (blue) can be categorized into three groups, i.e., a close-packed hexagon feature in the center (angular spacing of  $60^\circ$  between two main directions of **a** and **b**) and two slightly skewed features on the border and corner. The packing mismatch inside this top layer is evident with defects such as vacancy (filled yellow circle), edge dislocation (yellow T mark), and grain boundary (straight yellow line). Even though similar defects can also be found in the bottom layer (red) by splitting the single layer into three groups, the center of the layer clearly has adopted its own orientation freedom in packing. Particularly, the left side of the group rotated  $27.5^\circ$  from **a**, whereas the right side rotated  $19.7^\circ$  from **b**. Since this rotation change from left to right is quite sudden, both the edge dislocation and the grain boundary along the top boundary must have contributed to this variation. As a result, two clearly different Moiré features (patches 3 and 4) are revealed in Figure 6B, where no regular packing or ordering was found in the domain boundaries. However, when a grain boundary does not exist between the patches, for instance, group 2 vs the center one in the top layer, as well as group 1' vs the center one in the bottom layer, only a slight variation in orientation or packing is observed between the groups in the same layer. Such a gradual change coupled with a grain-boundary-induced abrupt

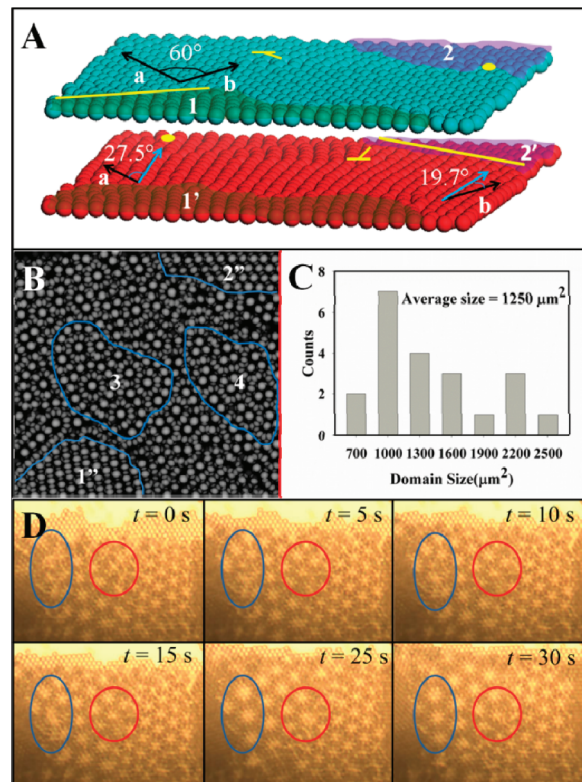


**Figure 6.** (A) 3D bilayer model of our hexagonal polymorph. Top and bottom layers are separated for clear viewing. (B) Top view of the Moiré patterns after overlapping both layers. (C) Domain size distribution of our observed Moiré patterns (data include those from movie clips). Domains (e.g.,  $1 + 1' \Rightarrow 1''$ ,  $2 + 2' \Rightarrow 2''$ ) resulted from the coupling of different crystal orientations between the top and bottom layers. Different crystal orientations within each layer are caused by defects, which are all marked yellow. The dot stands for vacancy, the “T” shape denotes edge dislocation, and the straight line for grain boundary. (D) Snapshots of the disorder–order phase transitions within a domain. During the phase transitions, microbeads along the rim of the top layer (without clear Moiré pattern; highlighted by two solid circles) can regroup into close-packed features (showing a clear Moiré pattern). This disorder–order transition occurs during the crystal growth process and can take tens or hundreds of seconds.

discontinuity in the neighboring layer apparently have released the rotation freedom that is demanded by a multifold symmetry in Moiré patterns. Thus, overlapped groups showed only a small translation or linear shift, producing two patches ( $1''$  and  $2''$ ) of necklace-like features as in Figure 6B. In this case, these domains are sitting next to those high symmetry Moiré neighbors, where limited packing ordering can still be spotted among the boundaries. Overall, unlike the regular hexagonal packing where the top beads always sit in the triple hollow sites, our observed bilayer crystal showed multiple ways of packing where abundant defects are believed to play a major role for the polymorphs. Due to this abundance in domain boundaries, our average domain size is rather small, ca.  $35 \mu\text{m}$  by  $35 \mu\text{m}$  or an area of  $1250 \mu\text{m}^2$  (Figure 6C). Interestingly, these imperfectly grown domains are found with capabilities to remediate. The *jp211369r\_si\_004.mpg* file in the Supporting Information shows an example where a disorder-to-order transition occurs when the system undergoes a sudden change from slow to fast flow. A sequence of snapshots (taken from *jp211369r\_si\_004.mpg*, Supporting Information) is shown in

Figure 6D. At  $t = 0$  s, near the rim of the top layer, microbeads are not packed well. Under a sudden acceleration of the capillary flow, these loosely packed beads gradually adjust their positions and become close-packed. Eventually (at  $t = 30$  s), much ordered Moiré patterns are formed.

Finally, we note that we have modeled the microbeads effectively as hard spheres. In reality, the bead–bead interactions are mainly through the van der Waals force, while the bead–water interactions are mainly through hydrogen bonding (because the surface of the silica beads is hydrophilic). When the beads are suspended in water, the hydrophilic surface of the beads will prevent the beads from sticking together (evidenced by the uniform distribution of the beads before the crystallization). In other words, the two forces act oppositely, and their sum plays little role compared to the gravity and viscous force. However, after the water is fully evaporated, we expect that the van der Waals interactions among microbeads would be comparable to the gravity and viscous forces, whose magnitude is on the order of  $5 \mu\text{N}$ . Indeed, we find that, when the bilayer crystal is dried, the van der Waals interaction becomes stronger so that the microbeads are pulled closer to each other. As a result, many regions of the bilayer crystal exhibit features with higher symmetry (see Figure S6, Supporting Information).

## 4. CONCLUSIONS

We have demonstrated real-time dynamics of growing bilayer crystals with Moiré patterns based on a unidirectional capillary flow in a slit pore. Unlike conventional open-ended drying or packing multiple layers using adsorbate–adsorbate and adsorbate–surface interactions, the introduction of the confined capillary flow provides a controllable factor to guide the crystallization of microbeads along the liquid–solid interface. Subsequent monolayer buckling or bead–monolayer collision promotes the growth of the observed bilayer crystal. Due to the rather thin nature of the bilayer structure, we are able to provide direct imaging of the crystal growth in a bead-by-bead and layer-by-layer fashion, as well as other intriguing phenomena, such as the formation of grain boundaries, disorder–order transitions, and the Moiré patterns. In addition, the imaging afforded by laser confocal microscopy facilitates our structural analysis of height-dependent polygonal tiling for the top monolayer. FFT of the triangle–rectangle tiling exhibits a 12-fold symmetry, which has implication to the formation of 2D quasicrystals. Since the bilayer crystals are built using a uniform building block, the capillary-flow induced crystal growth may find broad applications in making various bilayer crystals by design.

## ■ ASSOCIATED CONTENT

### Supporting Information

Schematic plot of the experimental setup, more detailed results, and the mechanics modeling. This material is available free of charge via the Internet at <http://pubs.acs.org>.

## ■ AUTHOR INFORMATION

### Corresponding Author

\*E-mail: ltan4@unl.edu (L.T.); xzeng1@unl.edu (X.C.Z.).

### Author Contributions

#These authors contributed equally to this work.

### Notes

The authors declare no competing financial interest.

## ■ ACKNOWLEDGMENTS

The authors gratefully acknowledge the financial support from the National Science Foundation, Army Research Office, Nebraska Center for Energy Science Research, and the Agilent Technologies Foundation. Z.G.C. appreciates many helpful discussions with Profs. Jiashi Yang (UNL), Zheng Li (Peking University), and John Barton (UNL).

## ■ REFERENCES

- (1) Stanley, H. E. *Introduction to Phase Transitions and Critical Phenomena*; Oxford: New York, 1971.
- (2) Papon, P.; Leblond, J.; Meijer, P. H. E. *The Physics of Phase Transitions: Concepts and Applications*; Springer: Berlin, 1999.
- (3) Onuki, A. *Phase Transition Dynamics*; Cambridge University: Cambridge, U.K., 2002.
- (4) Zheng, H. M.; Rivest, J. B.; Miller, T. A.; Sadler, B.; Lindenberg, A.; Toney, M. F.; Wang, L. W.; Kisielowski, C.; Alivisatos, A. P. *Science* **2011**, *333*, 206–209.
- (5) Anderson, V. J.; Lekkerkerker, H. N. W. *Nature* **2002**, *416*, 811–815.
- (6) Eldridge, M. D.; Madden, P. A.; Frenkel, D. *Nature* **1993**, *365*, 35–37.
- (7) Ramos, L.; Lubensky, T. C.; Dan, N.; Nelson, P.; Weitz, D. A. *Science* **1999**, *286*, 2325–2328.
- (8) Cheng, Z. D.; Russell, W. B.; Chaikin, P. M. *Nature* **1999**, *401*, 893–895.
- (9) Gasser, U.; Weeks, E. R.; Schofield, A.; Pusey, P. N.; Weitz, D. A. *Science* **2001**, *292*, 258–262.
- (10) Velikov, K. P.; Christova, C. G.; Dullens, R. P. A.; van Blaaderen, A. *Science* **2002**, *296*, 106–109.
- (11) Yethiraj, A.; van Blaaderen, A. *Nature* **2003**, *421*, 513–517.
- (12) Zhang, K. Q.; Liu, X. Y. *Nature* **2004**, *429*, 739–743.
- (13) Denkov, N. D.; Velev, O. D.; Kralchevsky, P. A.; Ivanov, I. B.; Yoshimura, H.; Nagayama, K. *Langmuir* **1992**, *8*, 3183–3190.
- (14) MacDonald, A. H.; Bistritzer, R. *Nature* **2011**, *474*, 453–454.
- (15) Singh, M. K.; Titus, E.; Goncalves, G.; Marques, P. A. A. P.; Bdikin, I.; Kholkin, A. L.; Gracio, J. J. A. *Nanoscale* **2010**, *2*, 700–708.
- (16) Xue, J. M.; Sanchez-Yamagishi, J.; Bulmash, D.; Jacquod, P.; Deshpande, A.; Watanabe, K.; Taniguchi, T.; Jarillo-Herrero, P.; Leroy, B. J. *Nat. Mater.* **2011**, *10*, 282–285.
- (17) Fujii, S.; Ryan, A. J.; Armes, S. P. *J. Am. Chem. Soc.* **2006**, *128*, 7882–7886.
- (18) Ishimasa, T.; Nissen, H. U.; Fukano, Y. *Phys. Rev. Lett.* **1985**, *55*, 511–513.
- (19) Stampfli, P. A. *Helv. Phys. Acta* **1986**, *59*, 1260–1263.
- (20) Leung, P. W.; Henley, C. L.; Chester, G. V. *Phys. Rev. B* **1989**, *39*, 446–458.
- (21) Widom, M. *Phys. Rev. Lett.* **1993**, *70*, 2094–2097.
- (22) Zeng, X. B.; Ungar, G.; Liu, Y. S.; Percec, V.; Dulcey, S. E.; Hobbs, J. K. *Nature* **2004**, *428*, 157–160.
- (23) Hayashida, K.; Dotera, T.; Takano, A.; Matsushita, Y. *Phys. Rev. Lett.* **2007**, *98*, 195502.
- (24) Mikhael, J.; Roth, J.; Helden, L.; Bechinger, C. *Nature* **2008**, *454*, 501–504.
- (25) Talapin, D. V.; Shevchenko, E. V.; Bodnarchuk, M. I.; Ye, X.; Chen, J.; Murray, C. B. *Nature* **2009**, *461*, 964–967.
- (26) Haji-Akbari, A.; Engel, M.; Keys, A. S.; Zheng, X. Y.; Petschek, R. G.; Palffy-Muhoray, P.; Glotzer, S. C. *Nature* **2009**, *462*, 773–777.
- (27) Fischer, S.; Exner, A.; Zielske, K.; Perlich, J.; Deloudi, S.; Steurer, W.; Lindner, P.; Forster, S. *Proc. Natl. Acad. Sci. U.S.A.* **2011**, *108*, 1810–1814.
- (28) Weitz, D. A.; Russel, W. B. *MRS Bull.* **2004**, *29*, 82–83.
- (29) Zhao, M. Q.; Crooks, R. M. *Angew. Chem., Int. Ed.* **1999**, *38*, 364–366.
- (30) Bohr, M. T. *IEEE Trans. Nanotechnol.* **2002**, *1*, 56–62.
- (31) Akahane, Y.; Asano, T.; Song, B. S.; Noda, S. *Nature* **2003**, *425*, 944–947.

- (32) Shalaev, V. M.; Cai, W. S.; Chettiar, U. K.; Yuan, H. K.; Sarychev, A. K.; Drachev, V. P.; Kildishev, A. V. *Opt. Lett.* **2005**, *30*, 3356–3358.
- (33) Schurig, D.; Mock, J. J.; Justice, B. J.; Cummer, S. A.; Pendry, J. B.; Starr, A. F.; Smith, D. R. *Science* **2006**, *314*, 977–980.
- (34) Lee, S.; Bluemle, M. J.; Bates, F. S. *Science* **2010**, *330*, 349–353.
- (35) Kishimoto, S.; Yamauchi, Y. *Phys. Chem. Chem. Phys.* **2009**, *11*, 5554–5557.
- (36) Yamauchi, Y.; Nagaura, T.; Takai, K.; Suzuki, N.; Sato, K.; Fukata, N.; Inoue, S.; Kishimoto, S. *J. Phys. Chem. C* **2009**, *113*, 9632–9637.
- (37) Glotzer, S. C.; Engel, M. *Nature* **2011**, *471*, 309–310.
- (38) White, F. M. *Viscous Fluid Flow*; McGraw-Hill: New York, 2006.
- (39) Chen, Z. G.; Liu, M. Z.; Liu, G. Y.; Tan, L. *Appl. Phys. Lett.* **2009**, *95*, 223104.